

Endothelial protein C receptor promotes retinal neovascularization through heme catabolism

Received: 29 March 2024

Accepted: 3 February 2025

Published online: 13 February 2025

 Check for updates

Hongyuan Song^{1,2,3,4,15}  , Qing Li^{1,5,15}, Xiao Gui^{1,6,15}, Ziyu Fang^{7,15}, Wen Zhou^{1,15}, Mengzhu Wang¹, Yuxin Jiang^{2,8}, Ajun Geng^{9,10}, Xi Shen¹¹, Yongxuan Liu¹, Haorui Zhang¹, Zheng Nie¹, Lin Zhang¹, Huimin Zhu¹, Feng Zhang¹² , Xuri Li¹², Fanyan Luo¹³ , Hongjian Zhang^{4,14} , Wei Shen¹  & Xiaodong Sun^{2,3,8} 

Pathological retinal neovascularization (RNV) is one of the leading causes of blindness worldwide; however, its underlying mechanism remains unclear. Here, we found that the expression of endothelial protein C receptor (*Epcr*) was increased during RNV, and its ligand was elevated in the serum or vitreous body of patients with proliferative diabetic retinopathy. Deleting endothelial *Epcr* or using an EPCR-neutralizing antibody ameliorated pathological retinal angiogenesis. EPCR promoted endothelial heme catabolism and carbon monoxide release through heme oxygenase 1 (HO-1). Inhibition of heme catabolism by deleting endothelial *Ho-1* or using an HO-1 inhibitor suppressed pathological angiogenesis in retinopathy. Conversely, supplementation with carbon monoxide rescued the angiogenic defects after endothelial *Epcr* or *Ho-1* deletion. Our results identified EPCR-dependent endothelial heme catabolism as an important contributor to pathological angiogenesis, which may serve as a potential target for treating vasoproliferative retinopathy.

Pathological retinal neovascularization (RNV) is a major cause of vision loss worldwide^{1,2}. The most common causes include diabetic retinopathy, retinopathy of prematurity (ROP), and retinal vein occlusion, which affect millions of people^{3–5}. The aberrant vessel growth usually leads to macular edema, fibrotic scarring, and retinal detachment^{2,6}.

These conditions are the primary causes of blindness in working-age and pediatric populations in developed countries^{6,7}. Endothelial cells (ECs) rarely proliferate and remain in a quiescent state in the adult organism, whereas uncontrolled proliferation of ECs is initiated and drives aberrant vessel growth under pathological stimuli⁸. Vascular

¹Department of Ophthalmology, Shanghai Changhai Hospital, Shanghai, China. ²Department of Ophthalmology, Shanghai General Hospital, Shanghai Jiao Tong University School of Medicine, Shanghai, China. ³National Clinical Research Center for Ophthalmic Diseases, Shanghai, China. ⁴Oriental Pan-Vascular Devices Innovation College, University of Shanghai for Science and Technology, Shanghai, China. ⁵The Affiliated Eye Hospital of Nanjing Medical University, Nanjing, China. ⁶Department of Ophthalmology, Yuanwang Hospital, Wuxi, China. ⁷Department of Urology, Shanghai Changhai Hospital, Shanghai, China. ⁸Shanghai Key Laboratory of Fundus Diseases, Shanghai, China. ⁹Key Laboratory of Systems Health Science of Zhejiang Province, School of Life Science, Hangzhou Institute for Advanced Study, Hangzhou, China. ¹⁰New Cornerstone Science Laboratory, State Key Laboratory of Cell Biology, CAS Center for Excellence in Molecular Cell Science, Institute of Biochemistry and Cell Biology, Chinese Academy of Sciences, University of Chinese Academy of Sciences, Shanghai, China. ¹¹Department of Ophthalmology, Ruijin Hospital, Shanghai Jiao Tong University School of Medicine, Shanghai, China. ¹²State Key Laboratory of Ophthalmology, Zhongshan Ophthalmic Center, Sun Yat-sen University, Guangdong Provincial Key Laboratory of Ophthalmology and Visual Science, Guangzhou, China. ¹³Department of Cardiac Surgery, Xiangya Hospital, Central South University, Changsha, China. ¹⁴Shidong Hospital Affiliated to University of Shanghai for Science and Technology, 999 Shiguang Road, Shanghai, China. ¹⁵These authors contributed equally: Hongyuan Song, Qing Li, Xiao Gui, Ziyu Fang, Wen Zhou. ✉ e-mail: hongyuansong@hotmail.com; drly@csu.edu.cn; hongjian_zhang@usst.edu.cn; shenwei@smmu.edu.cn; xdsun@sjtu.edu.cn

endothelial growth factor (VEGF) is extensively studied in the regulation of EC proliferation and angiogenesis^{9,10}. Anti-VEGF regents are first-line therapy for RNV, but resistance occurs in certain patients^{11,12}. Hence, it is necessary to identify novel therapeutic targets of RNV.

Endothelial protein C receptor (EPCR, also known as PROCR) is a single-pass transmembrane glycoprotein expressed in ECs and stem cells^{13,14}. In addition to its anti-coagulation role¹⁵, EPCR mediates intracellular signaling of activated protein C (APC)¹⁶. Activation of downstream protein kinase B (AKT) promotes cell growth, improves cardiac function, and favors tumor progression^{16–20}. Lineage tracing of *Epcr*-positive cells indicate that *Epcr* is specifically expressed in the ECs of the retinal vasculature²¹. *Epcr* transcription is activated in the retinal vessels during the angiogenic expansion stage but not during the quiescent stage²¹. Ablation of *Epcr*-positive cells leads to delayed retinal vascular expansion in postnatal mice, suggesting a role for EPCR in retinal angiogenesis²². However, the role of EPCR in RNV pathology remains unclear.

This study found that *Epcr* transcription was activated in ECs during RNV. Conditional knockout of *Epcr* in ECs or using an EPCR-neutralizing antibody ameliorated pathological RNV. Further data showed that EPCR affected heme catabolism by regulating heme oxygenase 1 (HMOX1, also known as HO-1). Conditional knockout of *Ho-1* in ECs or treatment with an HO-1 enzymatic inhibitor suppressed pathological angiogenesis in retinopathy. Carbon monoxide-releasing molecule-3 (CORM3) partially rescued the reduced neovascularization caused by the deletion of endothelial *Epcr* and *Ho-1*, indicating a role for carbon monoxide (CO). Clinically, levels of APC, which is an EPCR ligand, were elevated in proliferative diabetic retinopathy (PDR) patients' serum and vitreous body. These results indicate that EPCR-dependent endothelial heme catabolism is an important contributor to RNV.

Results

EPCR is highly expressed in retinal ECs during RNV

The mouse model of oxygen-induced retinopathy (OIR) serves as a proxy for human pathological RNV, including PDR and ROP²³. The neovascular response peaked on postnatal day 17 (P17) when the mice were returned to room air for five days (Fig. 1a). To identify the potential genes involved in pathological neovascularization, we performed transcriptomic analyses of the retinas of P17 mice of OIR (GSE241239). To minimize the RNA-seq bias, we further analyzed transcriptomic data from two other independent studies (GSE194176 and GSE158799)^{24,25}. A combined analysis revealed 303 upregulated genes (Fig. 1b, c). Among these candidate genes, we decided to focus on *Epcr* because EPCR was reported to be specifically detected on the surface of vascular ECs and stem cells^{13,14}. Further data confirmed that *Epcr* expression was upregulated in the retinas of P17 mice in the OIR (Fig. 1d, e). We sorted ECs from the mouse retina to evaluate the expression of *Epcr* in the retinal vasculature. Endothelial *Epcr* expression was much higher in the OIR group than in the control group (Fig. 1f, g).

Next, we examined the expression pattern of EPCR in the retina. Immunofluorescence staining with an anti-EPCR antibody showed that EPCR was selectively detected in the retinal ECs of P17 mice under physiological conditions (Supplementary Fig. 1a). In the OIR model, EPCR was detected only in retinal ECs, and the fluorescence intensity of EPCR signals was much higher in the neovascular tufts (Supplementary Fig. 1b, c). *Epcr*-CreER^{T2} (also known as *Procr*-CreER^{T2}) mice were previously used to mark proliferative ECs in the retinal vasculature²¹. Here, we used *Epcr*-CreER^{T2} and *Rosa26*^{tdT} mice to perform genetic lineage tracing of *Epcr*-positive cells in the retina of P17 mice. Tamoxifen (TAM) was administered for three consecutive days at P10, P11, and P12, and the retina was analyzed at P17 (Supplementary Fig. 1d). Under physiological conditions, a very small proportion of *Epcr*⁺ cells were observed (Fig. 1h). There was a large proportion of *Epcr*⁺ cells in the

retina of OIR mice, and *Epcr*⁺ cells mainly colocalized with neovascular tufts (Fig. 1h, i, Supplementary Fig. 1e). These data indicated that hypoxia significantly increased the transcription of *Epcr*. We also assessed the protein levels of EPCR in the retina of db/db mice with early-stage diabetes. The data showed that there was no difference in the protein levels of EPCR between db/db mice and db/m mice (Supplementary Fig. 1f–h). Hypoxia is also known to play a vital role in the retinal vascular development process²⁶. Therefore, the expression pattern of EPCR in the retinal vasculature of postnatal mice was then assessed. Immunofluorescence staining with anti-EPCR showed that the levels of EPCR were much higher in the margin of the retinal vasculature (Supplementary Fig. 1i). Consistent data were acquired using *Epcr*-CreER^{T2} and *Rosa26*^{tdT} mice (Supplementary Fig. 1j, k). Collectively, these data suggest that EPCR is specifically detected in ECs of the retina and is upregulated in neovascularization in the OIR model and during retinal vascular expansion.

EPCR activates downstream signaling pathways by binding to its ligands. Thus, we measured the serum concentrations of APC, a major ligand for EPCR, in OIR mice. The data showed that the levels of APC in the serum of OIR mice were higher than those in control mice (Fig. 1j). To evaluate whether the findings in mice hold promise for human patients with RNV, we investigated the levels of APC in the vitreous humor and serum in patients with PDR. The concentrations of APC in the vitreous humor and serum were significantly higher in patients with PDR than in the control with a macular hole or idiopathic epiretinal membrane (Fig. 1k, l).

EPCR contributes to RNV in vivo and in vitro

To determine the role of EPCR in RNV, we intercrossed the *Cdh5*-CreER^{T2} mouse with *Epcr*^{fllox/fllox} mouse to generate EC-specific *Epcr* KO mice (*Epcr*^{ΔEC}). The protein levels of EPCR were almost completely ablated in ECs sorted from *Epcr*^{ΔEC} mice (Supplementary Fig. 2a, b). Cre toxicity has been reported in another study²⁷, whereas our data showed that this mice strain did not cause vascular changes in the OIR model (Supplementary Fig. 2c–e). To assess the role of EPCR in pathological RNV, we examined the changes in the retinal vasculature of *Epcr*^{ΔEC} mice of OIR at P17. Our data showed that the area of neovascular tufts in the retina of *Epcr*^{ΔEC} mice was smaller than that in *Epcr*^{WT} mice (Fig. 2a, b). In contrast, the avascular area in *Epcr*^{ΔEC} mice's retina was larger than that in *Epcr*^{WT} mice (Fig. 2a, c). Furthermore, we used 5-ethynyl-2'-deoxyuridine (EdU) to label proliferative cells in the retina and used E26 transformation-specific (ETS)-related gene (ERG) as an EC marker. The result showed that EdU⁺ ECs in the retina decreased significantly in *Epcr*^{ΔEC} mice compared to *Epcr*^{WT} mice (Fig. 2d, e). Retinal vascular leakage was also attenuated in *Epcr*^{ΔEC} mice's retina compared to the retina of *Epcr*^{WT} mice (Supplementary Fig. 2f, g). Meanwhile, the data indicated that the deletion of endothelial *Epcr* did not affect the mature physiological angiogenesis of mice at P17 (Supplementary Fig. 2h, i). These in vivo results suggest that upregulated EPCR in pathological vasculature drives EC growth and angiogenesis in OIR.

Next, we determined the effect of *Epcr* deletion on retinal vascular expansion in postnatal retinas. EC-specific deletion of *Epcr* led to a sparse vascular network and reduced radial expansion of the superficial retinal vascular plexus (Supplementary Fig. 3a, b). Tip cells' filopodia and branch points were decreased in the retina of endothelial *Epcr* KO mice (Supplementary Fig. 3c–e). Meanwhile, EC proliferation was also significantly inhibited in *Epcr*^{ΔEC} mice (Supplementary Fig. 3f, g).

To further evaluate the impact of elevated EPCR on angiogenesis, we used an adenovirus to overexpress EPCR and assessed the angiogenic behavior of ECs in vitro. EPCR adenovirus treatment significantly increased the protein levels of EPCR in ECs, which promoted EC proliferation in an EdU staining assay (Fig. 2f, g, Supplementary Fig. 3h). A three-dimensional endothelial spheroid assay showed that the length

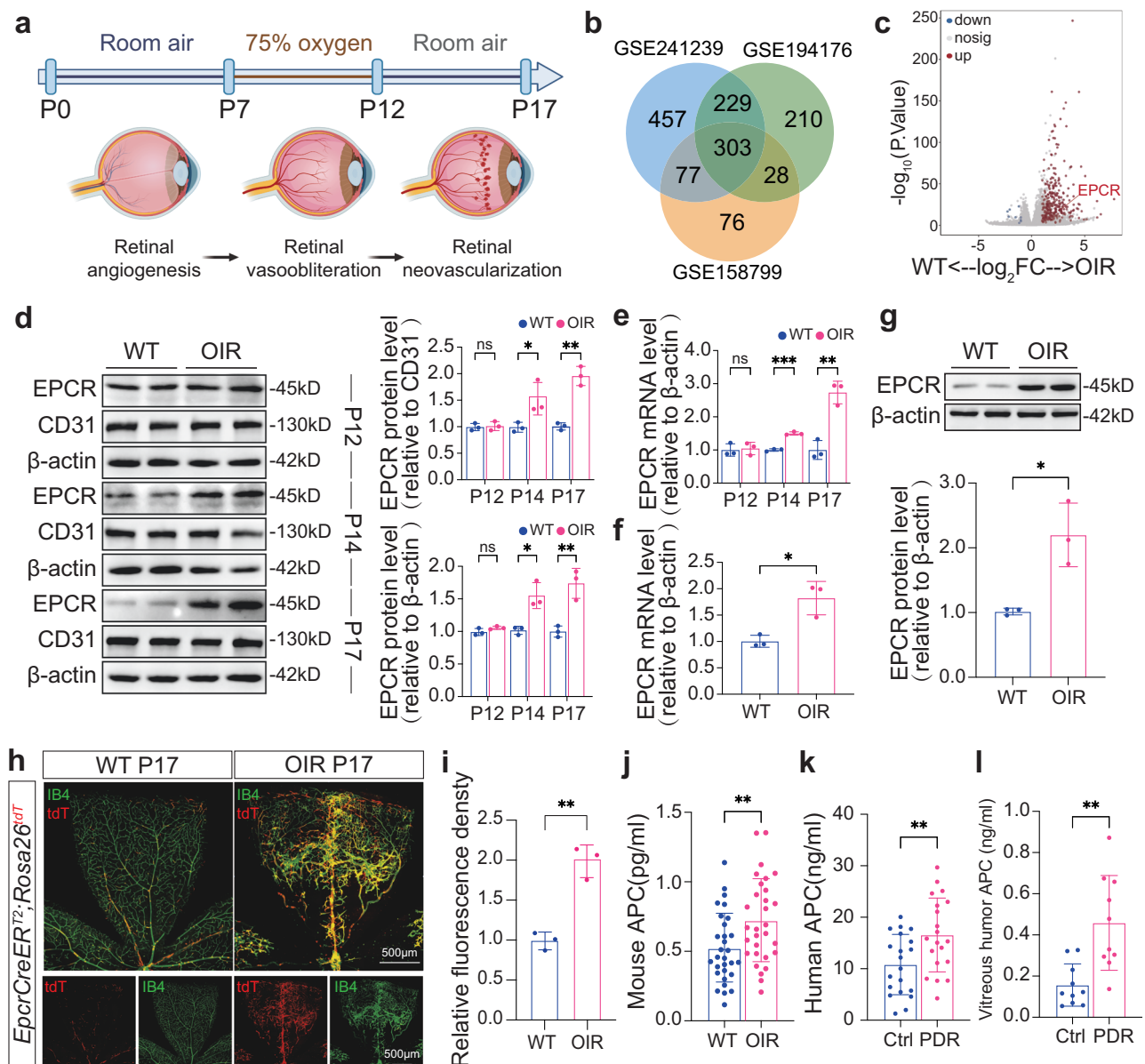


Fig. 1 | EPCR is specifically highly expressed in retinal neovascularization.

a Illustration of mouse model of OIR and different phases of retinopathy. Created in BioRender. Song, H. (2025) <https://BioRender.com/g81i639>. **b** Combined analysis of upregulated genes of three independent RNA-seq data in the retina of OIR mice. GSE241239 was performed in the present study. **c** Volcano plot of Log₂ fold-changed genes of three RNA-seq data. **d** The protein levels of EPCR in the retina throughout the progression of OIR. $n = 3$ biological replicates. Relative to β -Actin, Mean \pm SD, $p = 0.1864, 0.0102, 0.0064$ (two-tailed Student's t -test). Relative to CD31, Mean \pm SD, $p = 0.8608, 0.0362, 0.0010$ (two-tailed Student's t -test). **e** The mRNA levels of *Epcr* of the retina determined by qRT-PCR throughout the progression of OIR. $n = 3$ biological replicates. Mean \pm SD, $p = 0.7809, 0.0002, 0.0025$ (two-tailed Student's t -test). **f** FACS-isolated retinal endothelial cells from OIR mice at P17 showed increased expression of mRNA levels of *Epcr*. $n = 3$ biological

replicates. Mean \pm SD, $p = 0.0133$ (two-tailed Student's t -test). **g** The representative protein levels of EPCR in FACS-isolated retinal endothelial cells from OIR mice. $n = 3$ biological replicates. Mean \pm SD, $p = 0.0136$ (two-tailed Student's t -test). **h** Representative images of lineage tracing of *Epcr*-positive cells in P17 mice using *Epcr*-CreER^{T2}; *Rosa26*^{tdT} mice. Scale bar 500 μ m. **i** Quantification of the fluorescent intensity of *Epcr*-positive cells. $n = 3$ biological replicates. Mean \pm SD, $p = 0.0018$ (two-tailed Student's t -test). **j** WT ($n = 30$) and OIR ($n = 30$) mice serum APC levels were determined using ELISA. Mean \pm SD, $p = 0.0070$ (two-tailed Student's t -test). **k** Ctrl ($n = 20$) and PDR patients ($n = 20$) serum APC levels were determined with ELISA. Mean \pm SD, $p = 0.0080$ (two-tailed Student's t -test). **l** APC levels in Ctrl ($n = 10$) and PDR ($n = 10$) vitreous body were determined with ELISA. Mean \pm SD, $p = 0.0014$ (two-tailed Student's t -test). **** $p < 0.001$, ** $p < 0.01$, * $p < 0.05$. Source data are provided as a Source Data file.

of endothelial sprouts were increased in the *EPCR* adenovirus treatment group (Fig. 2h, i). Moreover, a wound scratch assay revealed that *EPCR* adenovirus-treated ECs were more motile than control adenovirus-treated ECs (Fig. 2j, k). Furthermore, the knockdown of *EPCR* using siRNA suppressed EC proliferation, migration, and sprouting (Fig. 2l–q, Supplementary Fig. 3i). Together with in vivo results, these data indicated that EPCR promotes vascular growth.

Pharmacological inhibition of EPCR ameliorates pathological retinal neovascularization

To evaluate the translational potential of targeting EPCR in anti-angiogenic therapy, we assessed the effects of a neutralizing antibody against EPCR on pathological angiogenesis in vitro and in vivo. We found that a single dose of EPCR antibody significantly reduced the area of neovascular tufts compared to the vehicle and anti-IgG groups

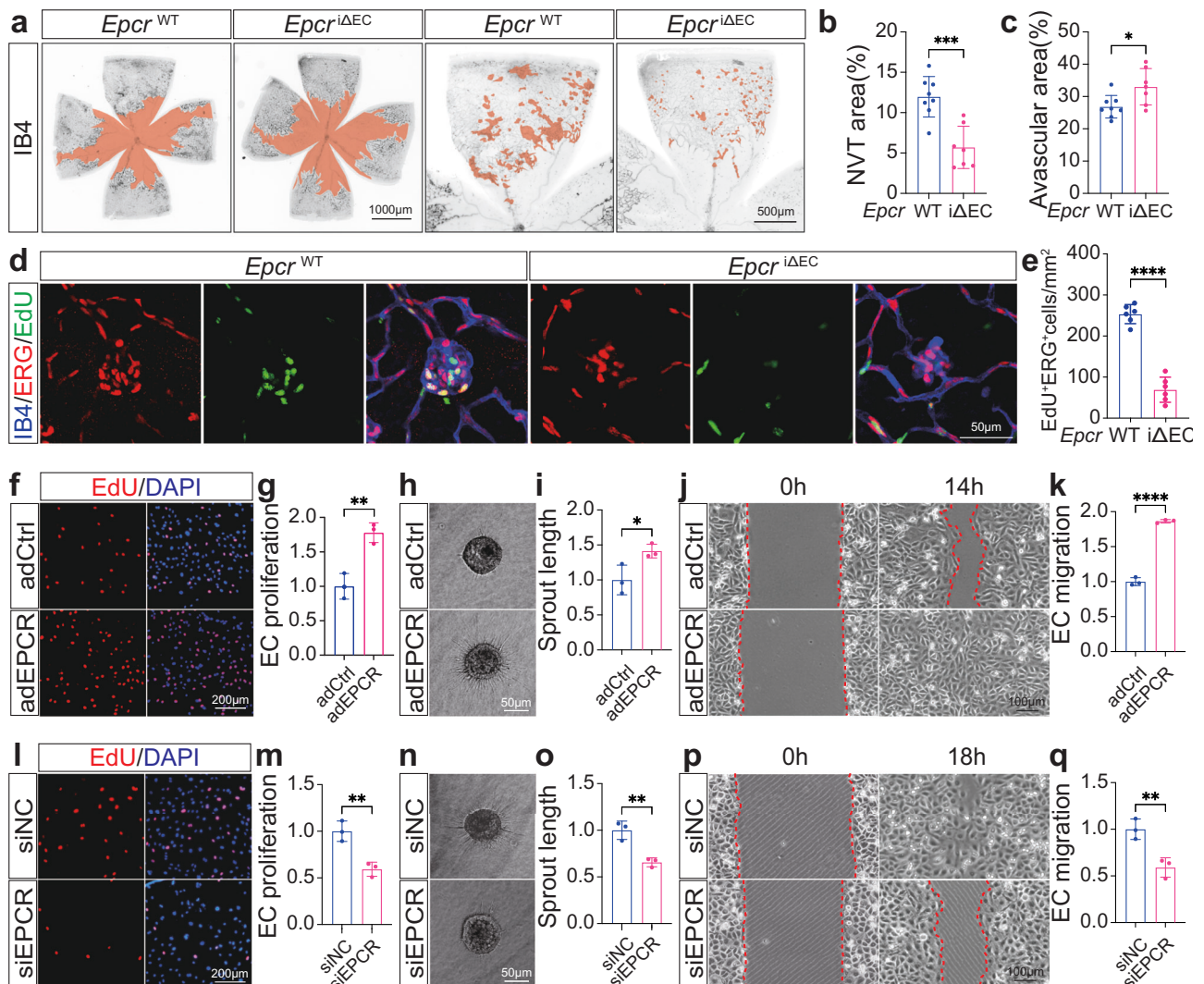


Fig. 2 | Loss of endothelial *Epcr* suppresses pathological RNV. **a** Representative images of retinal vasculature stained with IB4 in *Epcr*^{WT} and *Epcr*^{ΔEC} mice at P17 using the OIR mice model. The orange space indicates the avascular area for two left images and neovascular tufts for two right images. Scale bar 1000 μm and 500 μm. **b** Quantification of the area of neovascular tufts in *Epcr*^{WT} ($n = 8$) and *Epcr*^{ΔEC} ($n = 7$) mice. Mean \pm SD, $p = 0.0004$ (two-tailed Student's t-test). **c** Quantification of the avascular area in *Epcr*^{WT} ($n = 8$) and *Epcr*^{ΔEC} ($n = 7$) mice. Mean \pm SD, $p = 0.0218$ (two-tailed Student's t-test). **d** Immunofluorescence staining for IB4 (blue), E26 transformation-specific (ETS)-related gene (red), and EdU (green) in the retina of *Epcr*^{WT} and *Epcr*^{ΔEC} mice. Proliferating (E26 transformation-specific (ETS)-related gene and EdU double positive) ECs are shown in yellow. Scale bar 50 μm. **e** Quantification of the proliferating ECs in the retina of *Epcr*^{WT} ($n = 6$) and *Epcr*^{ΔEC} ($n = 6$) mice. Mean \pm SD, $p < 0.0001$ (two-tailed Student's t-test). **f** EdU-incorporation in *EPCR*-overexpressed human umbilical vein endothelial cells (HUVECs). DAPI (blue) was used to identify ECs nuclei. EdU (red) staining indicates proliferating ECs. Scale bar 200 μm. **g** Quantification of EdU-incorporation in *EPCR*-overexpressed HUVECs. $n = 3$ replicates, and the experiments were repeated 3 times. Mean \pm SD, $p = 0.0046$ (two-tailed Student's t-test). **h** Representative

images of HUVECs sprouting in *EPCR*-overexpressed HUVECs. Scale bar 50 μm. **i** Quantification of sprouts length in *EPCR*-overexpressed HUVECs. $n = 3$ replicates, and the experiments were repeated 3 times. Mean \pm SD, $p = 0.0375$ (two-tailed Student's t-test). **j** Wound healing of *EPCR*-overexpressed HUVECs. Scale bar 100 μm. **k** Quantification of wound healing ability in *EPCR*-overexpressed HUVECs. $n = 3$ replicates, and the experiments were repeated 3 times. Mean \pm SD, $p < 0.0001$ (two-tailed Student's t-test). **l** EdU-incorporation in *EPCR*-depleted HUVECs. DAPI (blue) is used to identify EC nuclei. EdU (red) staining indicates proliferating ECs. Scale bar 200 μm. **m** Quantification of EdU-incorporation in *EPCR*-depleted HUVECs. $n = 3$ replicates, and the experiments were repeated 3 times. Mean \pm SD, $p = 0.0061$ (two-tailed Student's t-test). **n** Representative images of sprouting in *EPCR*-depleted HUVECs. Scale bar 50 μm. **o** Quantification of sprouts length in *EPCR*-depleted HUVECs. $n = 3$ replicates, and the experiments were repeated 3 times. Mean \pm SD, $p = 0.0056$ (two-tailed Student's t-test). **p** Wound healing of *EPCR*-depleted HUVECs. Scale bar 100 μm. **q** Quantification of wound healing ability in *EPCR*-depleted HUVECs. $n = 3$ replicates, and the experiments were repeated 3 times. Mean \pm SD, $p = 0.0094$ (two-tailed Student's t-test). **** $p < 0.0001$, *** $p < 0.001$, ** $p < 0.01$, * $p < 0.05$. Source data are provided as a Source Data file.

(Fig. 3a, b). Whereas the avascular area remained unchanged after EPCR antibody treatment (Fig. 3a, c). Suppressed proliferation of ECs in retinal neovascular tufts was also observed after treatment with the EPCR antibody (Fig. 3d, e). Similar results were obtained in vitro as EPCR antibody treatment significantly inhibited EC proliferation, migration, and sprouting (Fig. 3f–k). These results were consistent with our findings using *Epcr*^{ΔEC} mice, suggesting the translational potential of anti-EPCR in the treatment of retinal neovascularization.

EPCR regulates the expression of HO-1 through NRF2/KEAP1

To reveal the possible molecular mechanisms underlying EPCR-regulated angiogenesis, we performed transcriptomic analyses of EPCR siRNA- or control siRNA-treated ECs (GSE249130, Supplementary Fig. 4a). These data were then combined and analyzed with the mice retina results with OIR (Supplementary Fig. 4b). Thirty genes were upregulated in the retina of OIR mice and downregulated in *Epcr*-depleted ECs (Fig. 4a). Among these genes, *Ho-1* was the most

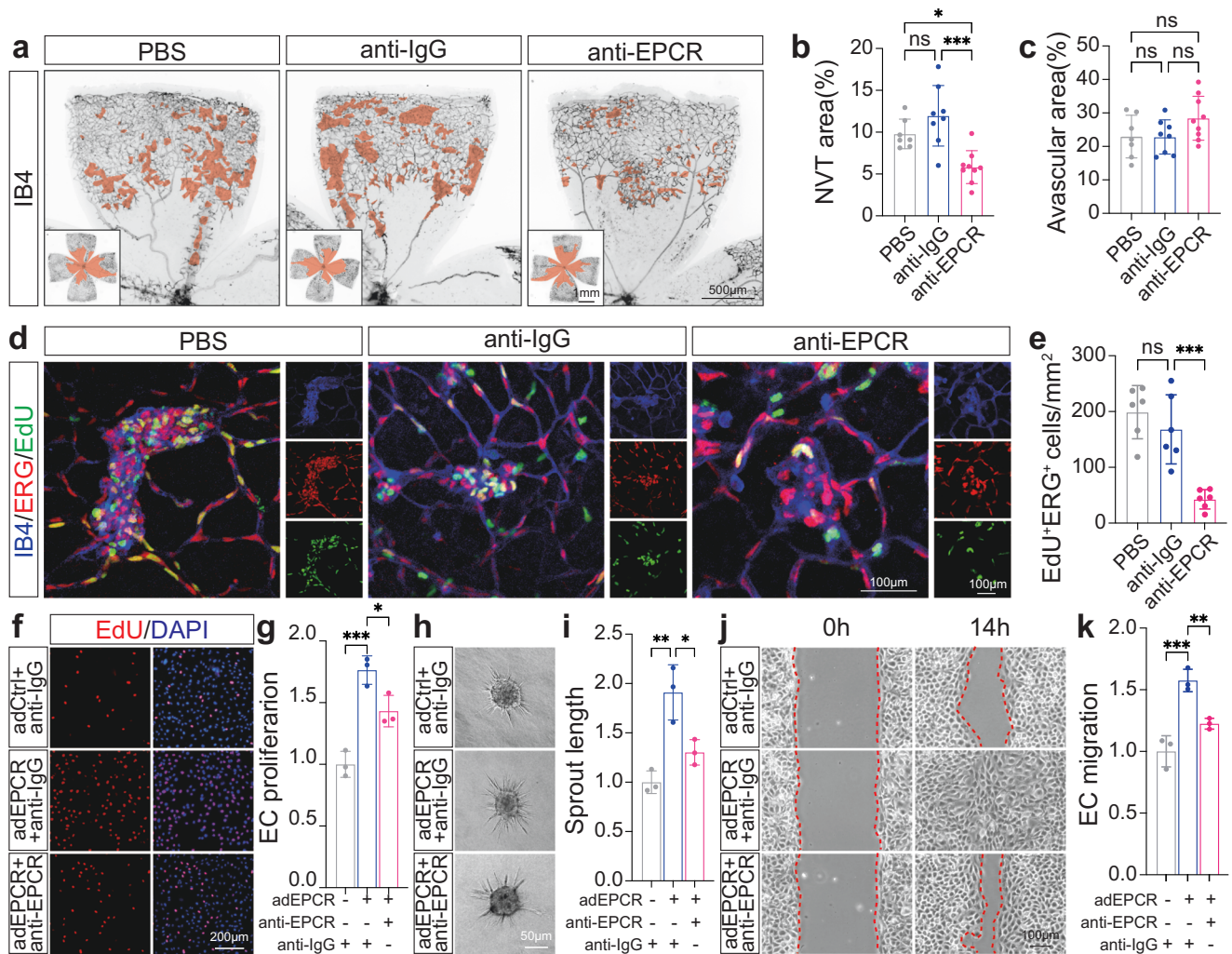


Fig. 3 | Pharmacological inhibition of EPCR attenuates pathological RNV.

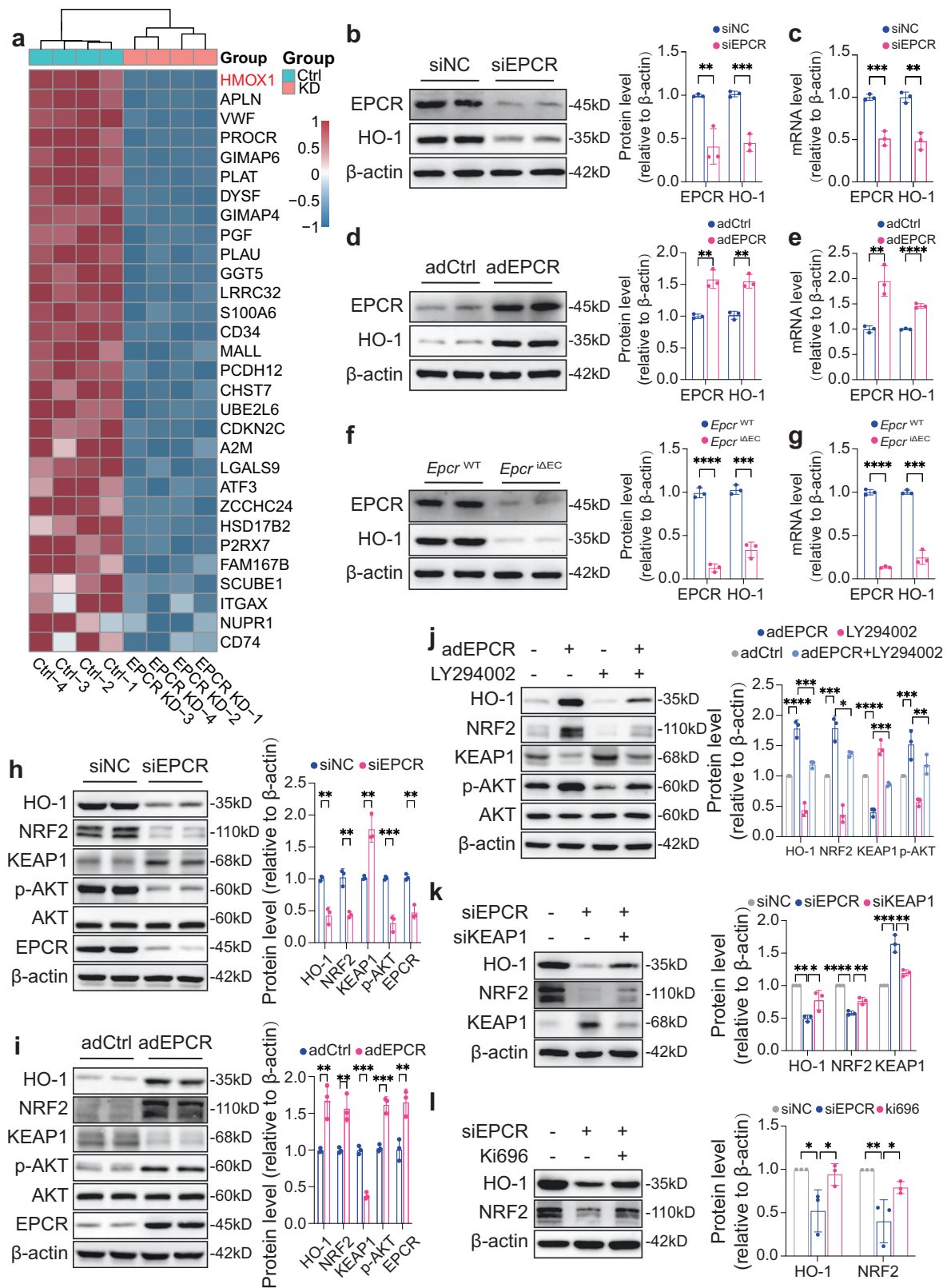
a Representative images of retinal vasculature stained with IB4 in PBS, anti-IgG and anti-EPCR-treated mice at P17 using the OIR mice model. The orange space indicates the avascular area for three lower images and neovascular tufts for three upper images. Scale bar 1 mm and 500 μ m. **b** Quantification of the area of neovascular tufts in PBS ($n = 7$), anti-IgG ($n = 8$) and anti-EPCR-treated ($n = 9$) mice. Mean \pm SD, $p = 0.2614$, 0.0164 , 0.0002 (one-way ANOVA with Tukey's multiple comparisons test). **c** Quantification of the avascular area in PBS ($n = 7$), anti-IgG ($n = 8$) and anti-EPCR-treated ($n = 9$) mice. Mean \pm SD, $p = 0.9994$, 0.1934 , 0.1622 (one-way ANOVA with Tukey's multiple comparisons test). **d** Immunofluorescence staining for IB4 (blue), E26 transformation-specific (ETS)-related gene (red), and EdU (green) in anti-EPCR-treated mice. Proliferating (E26 transformation-specific (ETS)-related gene and EdU double positive) ECs are shown in yellow. Scale bar 100 μ m. **e** Quantification of the proliferating ECs in PBS ($n = 6$), anti-IgG ($n = 6$) and anti-EPCR-treated ($n = 6$) mice. Mean \pm SD, $p = 0.4990$, 0.0008 (one-way ANOVA with

Tukey's multiple comparisons test). **f** EdU-incorporation in anti-EPCR-treated ECs (C166). DAPI (blue) is used to identify EC nuclei. EdU (red) staining indicates proliferating ECs. Scale bar 200 μ m. **g** Quantification of EdU-incorporation in anti-EPCR-treated ECs. $n = 3$ replicates, and the experiments were repeated 3 times. Mean \pm SD, $p = 0.0005$, $p = 0.0297$ (one-way ANOVA with Tukey's multiple comparisons test). **h** Representative images of anti-EPCR-treated ECs sprouting. Scale bar 50 μ m. **i** Quantification of sprouts length in anti-EPCR-treated ECs. $n = 3$ replicates, and the experiments were repeated 3 times. Mean \pm SD, $p = 0.0026$, $p = 0.0183$ (one-way ANOVA with Tukey's multiple comparisons test). **j** Wound healing of anti-EPCR-treated ECs. Scale bar 100 μ m. **k** Quantification of wound healing ability in anti-EPCR-treated ECs. $n = 3$ replicates, and the experiments were repeated 3 times. Mean \pm SD, $p = 0.0007$, $p = 0.0089$ (one-way ANOVA with Tukey's multiple comparisons test). $***p < 0.001$, $**p < 0.01$, $*p < 0.05$. Source data are provided as a Source Data file.

significantly affected (Fig. 4a). Increased mRNA and protein levels of *Ho-1* were confirmed in the retinas of OIR mice (Supplementary Fig. 4c, d). Further data showed that the expression of *Ho-1* was suppressed at the mRNA and protein levels in ECs treated with *EPCR* siRNA (Fig. 4b, c). Additionally, the expression of *Ho-1* was upregulated at the mRNA and protein levels in ECs treated with *EPCR* adenovirus (Fig. 4d, e). The expression of *Ho-1* in retinal ECs of OIR mice was then evaluated. We sorted ECs from the retina of OIR mice using flow cytometry. The results indicated that the expression of *Ho-1* in ECs was upregulated in the OIR group (Supplementary Fig. 4e, f). This was further confirmed by immunofluorescence staining. The expression of HO-1 in the physiological retina did not show an apparent pattern, while it was

highly expressed in neovascular tufts of OIR retinas (Supplementary Fig. 4g, h). Further data showed that the expression of *Ho-1* in ECs sorted from the retina of *Epcr*^{ΔEC} mice decreased compared with that in *Epcr*^{wt} mice (Fig. 4f, g). Collectively, these results suggested that HO-1 was a downstream molecule of EPCR in regulating angiogenesis.

AKT is recognized as a target of EPCR signaling²⁸. High EPCR expression or stimulation with APC usually leads to AKT activation^{16,19}. We found that overexpression of *EPCR* using an adenovirus promoted the activation of AKT, whereas silencing *EPCR* with siRNA inhibited AKT phosphorylation (Fig. 4h, i). Nuclear factor erythroid 2-related factor 2 (NRF2) is a ubiquitous transcription factor directly regulating HO-1²⁹. NRF2 is tightly regulated by Kelch-like ECH-associated protein 1



(KEAP1) through ubiquitination and proteasome-dependent degradation³⁰. Decreased expression of NRF2 and HO-1, and increased expression of KEAP1 were observed after *EPCR* knockdown in ECs (Fig. 4). Therefore, we assessed the effects of *EPCR* on the expression of KEAP1 and NRF2. Overexpression of *EPCR* in ECs promoted the levels of NRF2 and HO-1 and inhibited the expression of KEAP1 (Fig. 4i). Meanwhile, APC treatment stimulated the activation of

AKT and increased the expression of NRF2 and HO-1 while suppressing the expression of KEAP1 (Supplementary Fig. 4i).

AKT activates NRF2 in multiple cells^{31,32}. Our data showed that inactivating AKT with LY294002 (a PI3K inhibitor) blocked the effect of *EPCR* overexpression on NRF2, KEAP1, and HO-1 (Fig. 4j). Consistent results were observed when ECs were treated with APC (Supplementary Fig. 4j). These results suggested that AKT plays an important role

Fig. 4 | EPCR regulates the expression of HO-1 through NRF2/KEAP1. **a** Heatmap of genes (p -value) downregulated in RNA-seq data of *EPCR*-depleted HUVECs and upregulated in the RNA-seq data of the retinas from OIR mice. Heatmap was generated and analyzed using RNA-seq data from *EPCR*-depleted HUVECs. **b** Representative immunoblots and quantification for HO-1 levels in *EPCR*-depleted HUVECs. $n = 3$ biological replicates. Mean \pm SD, $p = 0.0077$, 0.0008 (two-tailed Student's t -test). **c** The mRNA levels of *HO-1* in *EPCR*-depleted HUVECs determined by qRT-PCR. $n = 3$ biological replicates. Mean \pm SD, $p = 0.0008$, 0.0016 (two-tailed Student's t -test). **d** Representative immunoblots and quantification for HO-1 levels of *EPCR* adenovirus-treated HUVECs. Mean \pm SD, $p = 0.0025$, 0.0016 (two-tailed Student's t -test). **e** The mRNA levels of *HO-1* in *EPCR* adenovirus-treated HUVECs determined by qRT-PCR. $n = 3$ biological replicates. Mean \pm SD, $p = 0.0058$, <0.0001 (two-tailed Student's t -test). **f** Representative immunoblots and quantification for HO-1 levels in ECs sorted from the retina of *Epcr*^{ΔEC} mice. $n = 3$ biological replicates. Mean \pm SD, $p < 0.0001$, $p = 0.0004$ (two-tailed Student's t -test). **g** The mRNA levels of *HO-1* in ECs sorted from the retina of *Epcr*^{ΔEC} mice. $n = 3$ biological replicates. Mean \pm SD, $p < 0.0001$, $p = 0.0001$ (two-tailed Student's t -test). **h** Representative immunoblots and quantification for HO-1,

NRF2, KEAP1, p-AKT(S473), and EPCR levels in *EPCR*-depleted HUVECs. $n = 3$ biological replicates. Mean \pm SD, $p = 0.017$, 0.0021 , 0.0031 , 0.0007 , 0.0014 (two-tailed Student's t -test). **i** Representative immunoblots and quantification for HO-1, NRF2, KEAP1, p-AKT(S473), and EPCR levels in *EPCR* adenovirus-treated HUVECs. $n = 3$ biological replicates. Mean \pm SD, $p = 0.0075$, 0.0063 , 0.0001 , 0.0008 , 0.0079 (two-tailed Student's t -test). **j** Representative immunoblots and quantification for HO-1, NRF2, KEAP1, and p-AKT(S473) levels in *EPCR* adenovirus and LY294002-treated HUVECs. $n = 3$ biological replicates. Mean \pm SD, $p < 0.0001$, $p = 0.0002$, 0.0002 , 0.0128 , <0.0001 , 0.0003 , 0.0003 , 0.0029 (one-way ANOVA with Tukey's multiple comparisons test). **k** Representative immunoblots and quantification for HO-1, NRF2 and KEAP1 levels in *EPCR*-depleted and *KEAP1*-depleted HUVECs. $n = 3$ biological replicates. Mean \pm SD, $p = 0.0013$, $p = 0.0221$, <0.0001 , 0.0015 , 0.0002 , 0.0013 (one-way ANOVA with Tukey's multiple comparisons test). **l** Representative immunoblots and quantification for HO-1 and NRF2 levels in *EPCR*-depleted and *KEAP1* inhibitor-treated HUVECs. $n = 3$ biological replicates. Mean \pm SD, $p = 0.0247$, 0.0395 , 0.0068 , 0.0426 (one-way ANOVA with Tukey's multiple comparisons test). **** $p < 0.0001$, *** $p < 0.001$, ** $p < 0.01$, * $p < 0.05$. Source data are provided as a Source Data file.

in mediating EPCR signaling. Furthermore, we observed that depleting the expression of *KEAP1* using siRNA rescued the downregulation of NRF2 and HO-1 caused by *EPCR* siRNA (Fig. 4k, Supplementary Fig. 4k). Consistent results were obtained after treatment with Ki696 (a KEAP1 inhibitor) (Fig. 4l). These data suggested that EPCR controlled HO-1 expression via the AKT-KEAP1-NRF2 pathway.

Considering the critical role of VEGF in promoting RNV, we assessed the effect of EPCR signaling on VEGF. The results showed that neither knockdown nor overexpressing *EPCR* affected the protein levels of VEGFA (Supplementary Fig. 5a, b). The data suggested that endothelial EPCR signaling might be VEGF-independent. BTB and CNC Homology 1 (BACH1) is a transcription factor that regulates oxidative stress response and heme metabolism²⁹. Stromal Cell-Derived Factor 1 (SDF1), also known as CXCL12, has been shown to promote angiogenesis through HO-1³³. Thus, we further evaluated the role of BACH1 and SDF1 in EPCR signaling. The results showed that depletion of *BACH1* in ECs could increase the protein levels of HO-1 (Supplementary Fig. 5c). However, the protein levels of BACH1 did not change in the retina of OIR mice compared to control mice (Supplementary Fig. 5d), and neither knockdown nor overexpressing *EPCR* affected the protein levels of BACH1 (Supplementary Fig. 5e, f). The data indicated that BACH1 did not participate in the endothelial EPCR signaling pathway. Consistent with a previous report^{34,35}, the results showed that the protein levels of SDF1 increased significantly in the retinal neovascularization in OIR mice (Supplementary Fig. 6a, b), and knockdown of *SDF1* decreased the expression of HO-1 (Supplementary Fig. 6c). SDF1 usually interacts with C-X-C motif chemokine receptor 4 and activates downstream AKT signaling pathways to promote angiogenesis³³. Knockdown of *EPCR* in ECs could suppress the expression of SDF1, while overexpression of *EPCR* could increase the expression of SDF1 (Supplementary Fig. 6d, e). These data suggested that EPCR might regulate the expression of SDF-1 through AKT signaling. This was further confirmed as ECs treated with LY294002 exhibited reduced SDF-1 expression (Supplementary Fig. 6f). However, the knockdown of *SDF1* did not reverse the increased expression of HO-1 induced by *EPCR* overexpression (Supplementary Fig. 6g). All these data suggested that EPCR regulated the expression of SDF-1 through of AKT signaling, and SDF-1 did not contribute to the expression of HO-1 regulated by EPCR.

Genetic ablation of endothelial *HO-1* attenuates angiogenesis

To evaluate the role of HO-1 in retinal angiogenesis, we bred *Cdh5-CreER*^{T2} mice with *HO-1*^{fllox/fllox} mice to generate EC-specific *HO-1* KO mice (*HO-1*^{ΔEC}). The deletion efficiency was determined using flow cytometry-sorted ECs, and the protein levels of HO-1 in ECs sorted from *HO-1*^{ΔEC} mice were significantly decreased (Supplementary Fig. 7a). The role of HO-1 in pathological retinal angiogenesis was then

determined in the OIR mice. Our data showed that the area of neovascular tufts in the retina of *HO-1*^{ΔEC} mice was smaller, while the avascular area in the retina of *HO-1*^{ΔEC} mice was larger than that in *HO-1*^{WT} mice (Fig. 5a–c). Furthermore, our results showed that EdU⁺ ECs decreased significantly in the retina of *HO-1*^{ΔEC} mice than in *HO-1*^{WT} mice (Fig. 5d, e).

Physiological retinal vascular development was also affected in *HO-1*^{ΔEC} mice. Deleting endothelial *HO-1* reduced radial expansion of the superficial retinal vascular plexus (Supplementary Fig. 7b, c). Meanwhile, the tip cells' filopodia and branch points were decreased in the retina of *HO-1*^{ΔEC} mice (Supplementary Fig. 7d–f). Additionally, EdU⁺ ECs decreased significantly in the retina of *HO-1*^{ΔEC} mice than in *HO-1*^{WT} mice (Supplementary Fig. 7g, h).

The role of HO-1 in angiogenesis was further assessed in vitro. First, the knockdown efficiency of *HO-1* siRNA was evaluated (Supplementary Fig. 7i). The EdU assay showed that silencing *HO-1* inhibited EC proliferation induced by the *EPCR* adenovirus (Fig. 5f, g). A three-dimensional endothelial spheroid assay was used to evaluate the angiogenic potential of ECs treated with *EPCR* adenovirus and *HO-1* siRNAs. Fewer and shorter sprouts were observed in *HO-1* siRNA-treated ECs than in *EPCR* adenovirus-treated ECs (Fig. 5h, i). Besides, ECs treated with *HO-1* siRNAs exhibited impaired migration ability compared to the *EPCR* adenovirus treatment group (Fig. 5j, k). We also assessed the effects of *HO-1* knockdown on ECs. The results showed that silencing *HO-1* suppressed EC proliferation, migration, and sprouting (Supplementary Fig. 7j–o). These results collectively revealed the vital role of HO-1 in developmental angiogenesis and RNV.

Endothelial heme catabolism impacts angiogenesis

HO-1 catalyzes heme degradation into CO, biliverdin, and iron³⁶. Catabolism of cytotoxic labile heme and the generation of CO exert cytoprotective effects³⁷. Thus, we further assessed whether the angiogenic role of HO-1 was mediated by its enzymatic function. Here, a heme oxygenase (both HO-1 and HO-2) enzymatic inhibitor, zinc protoporphyrin IX (ZnPPiX), was used to determine its effect on pathological RNV. The data showed that ZnPPiX treatment decreased the area of neovascular tufts in the retina and increased the avascular area (Fig. 6a–c). Besides, ZnPPiX suppressed EC proliferation as EdU⁺ retinal ECs decreased significantly in mice treated with ZnPPiX (Fig. 6d, e).

Next, we determined the effect of ZnPPiX on retinal vascular expansion. ZnPPiX treatment led to a sparse vascular network and reduced radial expansion of the superficial retinal vascular plexus (Supplementary Fig. 8a, b). The tip cells' filopodia and branch points were decreased in the retina of mice treated with ZnPPiX (Supplementary Fig. 8c–e). Meanwhile, ZnPPiX

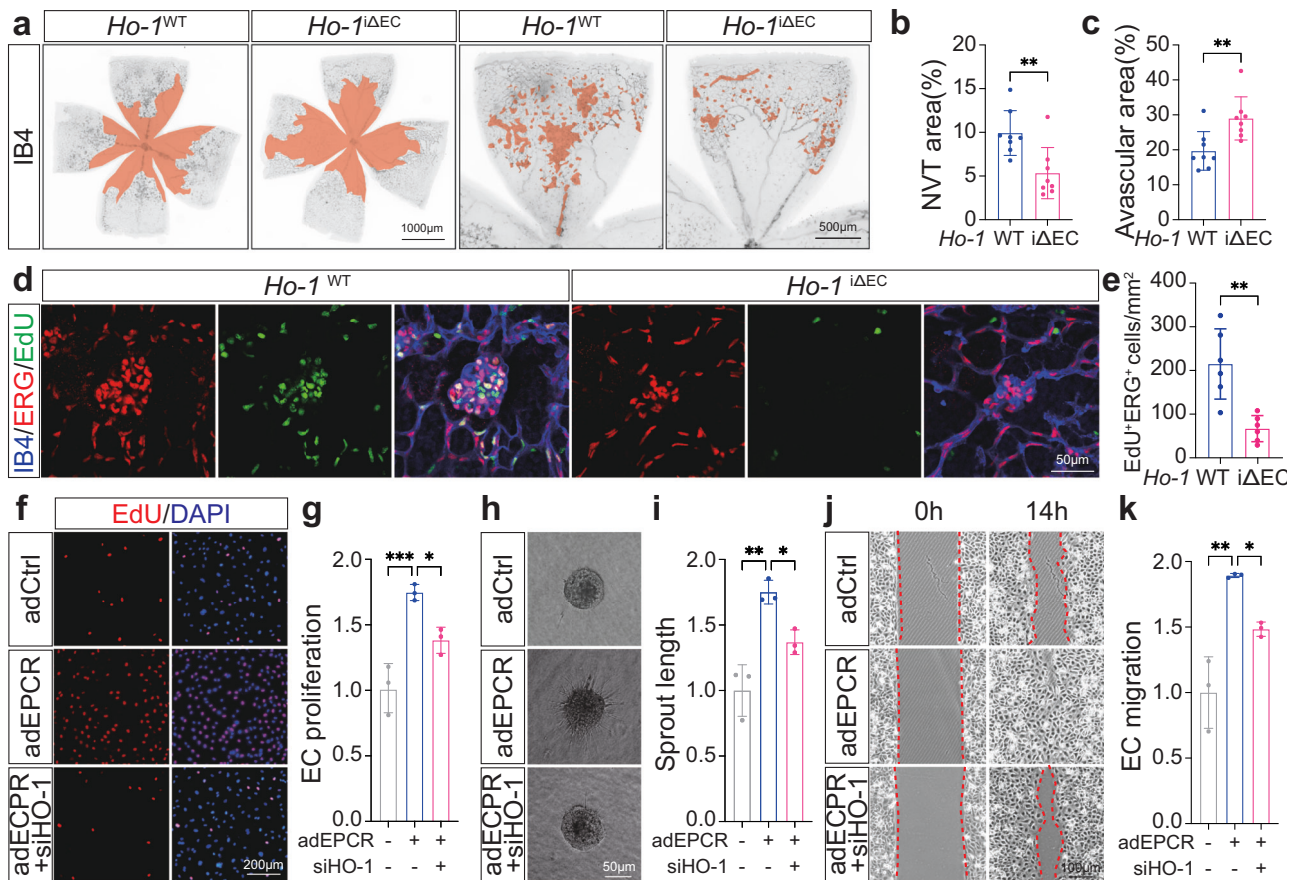


Fig. 5 | Endothelial deletion of *Ho-1* inhibits pathological RNV. **a** Representative images of retinal vasculature stained with IB4 in the retina of *Ho-1*^{WT} and *Ho-1*^{ΔEC} mice at P17 using the OIR mice model. The orange space indicates the avascular area for two left images and neovascular tufts for two right images. Scale bar 1000 μm and 500 μm. **b** Quantification of the area of neovascular tufts in *Ho-1*^{WT} (*n* = 8) and *Ho-1*^{ΔEC} (*n* = 8) mice. Mean ± SD, *p* = 0.0049 (two-tailed Student's *t*-test). **c** Quantification of the avascular area in *Ho-1*^{WT} (*n* = 8) and *Ho-1*^{ΔEC} (*n* = 8) mice. Mean ± SD, *p* = 0.0067 (two-tailed Student's *t*-test). **d** Immunofluorescence staining for IB4 (blue), E26 transformation-specific (ETS)-related gene (red), and EdU (green) in the retina of *Ho-1*^{WT} and *Ho-1*^{ΔEC} mice. Proliferating (E26 transformation-specific (ETS)-related gene and EdU double positive) ECs are shown in yellow. Scale bar 50 μm. **e** Quantification of the proliferating ECs in the retina *Ho-1*^{WT} (*n* = 6) and *Ho-1*^{ΔEC} (*n* = 6) mice. Mean ± SD, *p* = 0.0018 (two-tailed Student's *t*-test). **f** EdU-incorporation in HUVECs treated with *EPCR* adenovirus and *HO-1* siRNA. DAPI (blue) identifies ECs nuclei. EdU (red) staining indicates proliferating ECs. Scale bar

200 μm. **g** Quantification of EdU-incorporation in HUVECs treated with *EPCR* adenovirus and *HO-1* siRNA. *n* = 3 replicates, and the experiments were repeated 3 times. Mean ± SD, *p* = 0.0009, *p* = 0.0300 (one-way ANOVA with Tukey's multiple comparisons test). **h** Representative sprouting images in HUVECs treated with *EPCR* adenovirus and *HO-1* siRNA. Scale bar 50 μm. **i** Quantification of sprouts length in HUVECs treated with *EPCR* adenovirus and *HO-1* siRNA. *n* = 3 replicates, and the experiments were repeated 3 times. Mean ± SD, *p* = 0.0013, *p* = 0.0320 (one-way ANOVA with Tukey's multiple comparisons test). **j** Representative wound healing images in HUVECs treated with *EPCR* adenovirus and *HO-1* siRNA. Scale bar 100 μm. **k** Quantification of wound healing ability in HUVECs treated with *EPCR* adenovirus and *HO-1* siRNA. *n* = 3 replicates, and the experiments were repeated 3 times. Mean ± SD, *p* = 0.0012, *p* = 0.0471 (one-way ANOVA with Tukey's multiple comparisons test). ****p* < 0.001, ***p* < 0.01, **p* < 0.05. Source data are provided as a Source Data file.

significantly suppressed ECs proliferation in the retina (Supplementary Fig. 8f, g).

Further data showed that *EPCR*-induced cell proliferation, migration, and sprouting of ECs in vitro were inhibited by ZnPPiX (Fig. 6f–k). Additionally, we evaluated the effect of ZnPPiX on ECs treated with *HO-1* siRNA. The result showed that ZnPPiX did not affect EC proliferation, migration, and sprouting after *HO-1* knockdown (Supplementary Fig. 8h–m). These data indicated that endothelial heme catabolism contributes to *EPCR*-mediated RNV.

Heme catabolism-derived CO contributes to pathological angiogenesis

Endogenous CO is a signaling molecule that promotes tumor growth and angiogenesis^{38,39}. Heme catabolism in macrophages increases tumor angiogenesis through CO production, suggesting a role for CO in regulating angiogenesis³⁷. Here, we showed that pathological retinal neovascular tufts in carbon monoxide-releasing molecule-3

(CORM3)-treated *Ho-1*^{ΔEC} mice significantly increased compared with that in *Ho-1*^{ΔEC} mice, while the avascular area was decreased (Fig. 7a–c). Furthermore, the data showed that EdU⁺ ECs also increased significantly in the CORM3-treated retina of *Ho-1*^{ΔEC} mice than that in *Ho-1*^{ΔEC} mice (Fig. 7d, e). Pathological retinal neovascular tufts in CORM3-treated *Epcr*^{ΔEC} mice also significantly increased, and avascular area decreased compared with that in *Epcr*^{ΔEC} mice (Supplementary Fig. 9a–c). Consistent data were acquired for the number of EdU⁺ ECs (Supplementary Fig. 9d, e). Meanwhile, the role of other byproducts of heme catabolism was evaluated. The data showed that bilirubin and iron supplements did not reverse the vascular changes caused by endothelial *Epcr* deletion (Supplementary Fig. 10).

We then assessed the effect of CORM3 on postnatal retinal vasculature in *Ho-1*^{ΔEC} and *Epcr*^{ΔEC} mice. Treatment with CORM3 could rescue the sparse vascular network and increase the radial expansion of superficial retinal vascular plexus in *Ho-1*^{ΔEC} mice (Supplementary Fig. 11a, b). Compared with *Ho-1*^{ΔEC} mice, tip cells' filopodia and branch

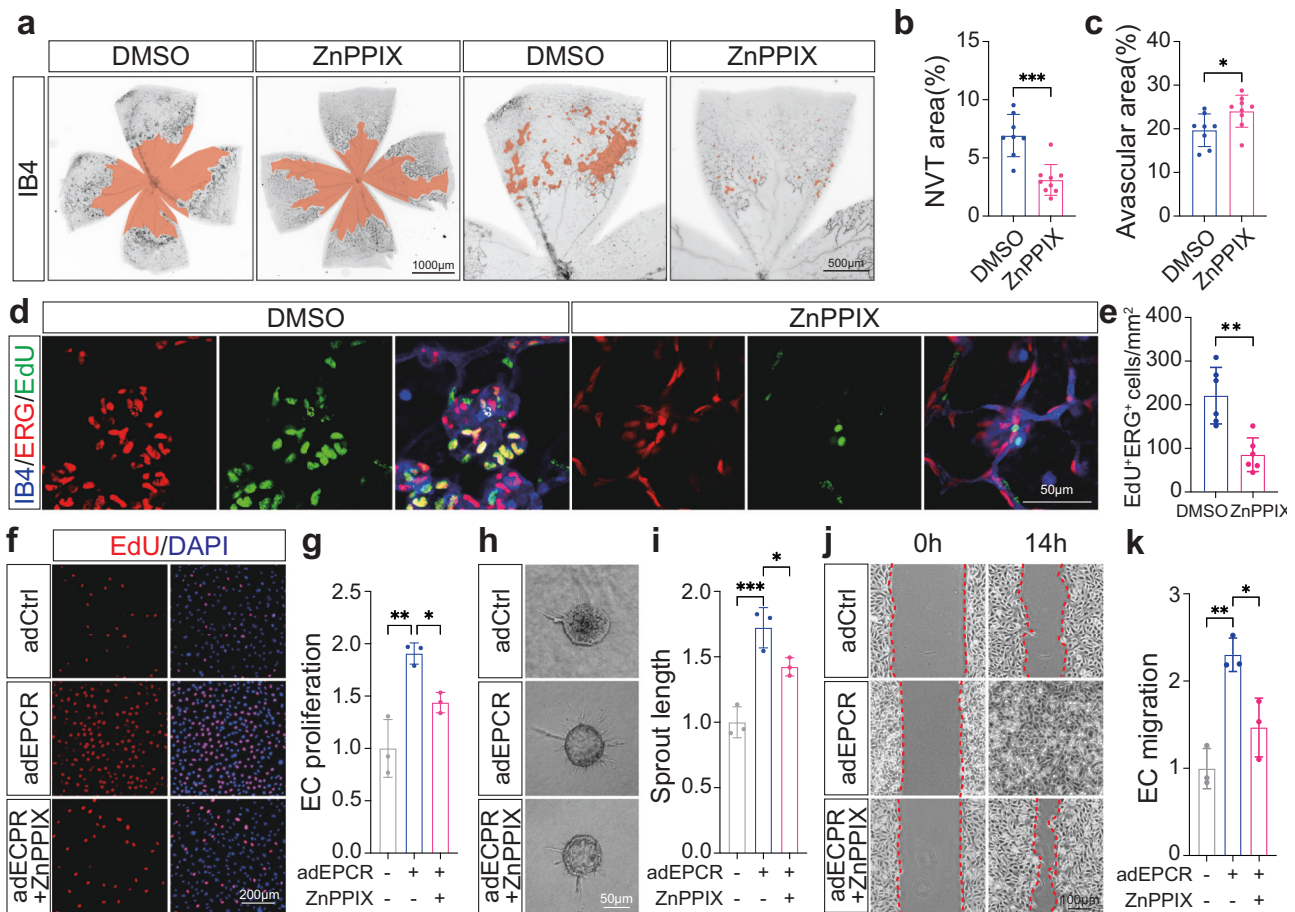


Fig. 6 | Endothelial heme catabolism inhibition ameliorates RNV.

a Representative images of retinal vasculature stained with IB4 in DMSO or ZnPPiX-treated mice at P17 using the OIR mice model. The orange space indicates the avascular area for two left images and neovascular tufts for two right images. Scale bar 1000 μ m and 500 μ m. **b** Quantification of the area of neovascular tufts in DMSO ($n = 8$) and ZnPPiX-treated ($n = 9$) mice. Mean \pm SD, $p = 0.0002$ (two-tailed Student's *t*-test). **c** Quantification of the avascular area in the retina of DMSO ($n = 8$) and ZnPPiX-treated ($n = 9$) mice. Mean \pm SD, $p = 0.0291$ (two-tailed Student's *t*-test). **d** Immunofluorescence staining for IB4 (blue), E26 transformation-specific (ETS)-related gene (red), and EdU (green) in the retina of DMSO and ZnPPiX-treated mice. Proliferating (E26 transformation-specific (ETS)-related gene and EdU double positive) ECs are shown in yellow. Scale bar 50 μ m. **e** Quantification of the proliferating ECs in the retina of DMSO ($n = 6$) and ZnPPiX-treated ($n = 6$) mice. Mean \pm SD, $p = 0.0013$ (two-tailed Student's *t*-test). **f** EdU-incorporation in *EPCR*

adenovirus and ZnPPiX-treated HUVECs. DAPI (blue) identifies EC nuclei. EdU (red) staining indicates proliferating ECs. Scale bar 200 μ m. **g** Quantification of EdU-incorporation in *EPCR* adenovirus and ZnPPiX-treated HUVECs. $n = 3$ replicates, and the experiments were repeated 3 times. Mean \pm SD, $p = 0.0020$, $p = 0.0422$ (one-way ANOVA with Tukey's multiple comparisons test). **h** Representative sprouting images of *EPCR* adenovirus and ZnPPiX-treated HUVECs. Scale bar 50 μ m. **i** Quantification of sprouts length in *EPCR* adenovirus and ZnPPiX-treated HUVECs. $n = 3$ replicates, and the experiments were repeated 3 times. Mean \pm SD, $p = 0.0008$, $p = 0.0498$ (one-way ANOVA with Tukey's multiple comparisons test). **j** Wound healing of *EPCR* adenovirus and ZnPPiX-treated HUVECs. Scale bar 100 μ m. **k** Quantification of wound healing ability in *EPCR* adenovirus and ZnPPiX-treated HUVECs. $n = 3$ replicates, and the experiments were repeated 3 times. Mean \pm SD, $p = 0.0021$, $p = 0.0184$ (one-way ANOVA with Tukey's multiple comparisons test). *** $p < 0.001$, ** $p < 0.01$, * $p < 0.05$. Source data are provided as a Source Data file.

points increased in the retina of *Ho-1*^{ΔEC} mice treated with CORM3 (Supplementary Fig. 11c–e). Consistent results were acquired in CORM3-treated *Epcr*^{ΔEC} mice (Supplementary Fig. 11f–j).

Furthermore, CORM3 rescued *HO-1* silence-caused inhibition of EC proliferation, migration, and sprouting (Fig. 7f–k). Additionally, the effect of CORM3 on *EPCR*-deleted ECs was evaluated. The results showed that *EPCR* silencing inhibited EC proliferation, migration, and sprouting, which was partially reversed after treatment with CORM3 (Supplementary Fig. 12a–f). These results suggested that CO was an important contributor to *EPCR*-dependent endothelial heme catabolism-regulated angiogenesis.

Discussion

Therapeutic strategies for RNV are effective, but off-target effect and resistance limit their efficacy^{12,40}. The reason is that these therapies cannot distinguish between healthy and pathological vessels. Our current study showed that *EPCR* was selectively detected in ECs of the

retina, and *EPCR* transcription was activated under angiogenic stimulus. Conditional deletion of *Epcr* in ECs or anti-*EPCR* neutralizing antibody treatment attenuated pathological retinopathy. Mechanistically, *EPCR*-controlled endothelial heme catabolism through HO-1 and heme catabolism-derived CO plays a vital role. Notably, the *EPCR* ligand levels were elevated in the vitreous body or serum of patients with PDR. These observations revealed the potential therapeutic value of targeting *EPCR* for suppressing pathological RNV (Fig. 8).

Here, we observed that the expression of *EPCR* was detected specifically in the retinal ECs and was upregulated in neovascular tufts using anti-*EPCR* staining. *EPCR* was not detected in retinal pigment epithelia, photoreceptor cells, or ganglion cells. Consistent with our previous work²¹, we found that *Epcr* transcription is activated during the vessel expansion stage in the retina. Meanwhile, *Epcr* transcription was activated in ECs during RNV using *Epcr*-CreER^{T2}; *Rosa26*^{dT} mice. These findings revealed that *EPCR* expression was selectively detected on retinal ECs and was upregulated under angiogenic stimulus.

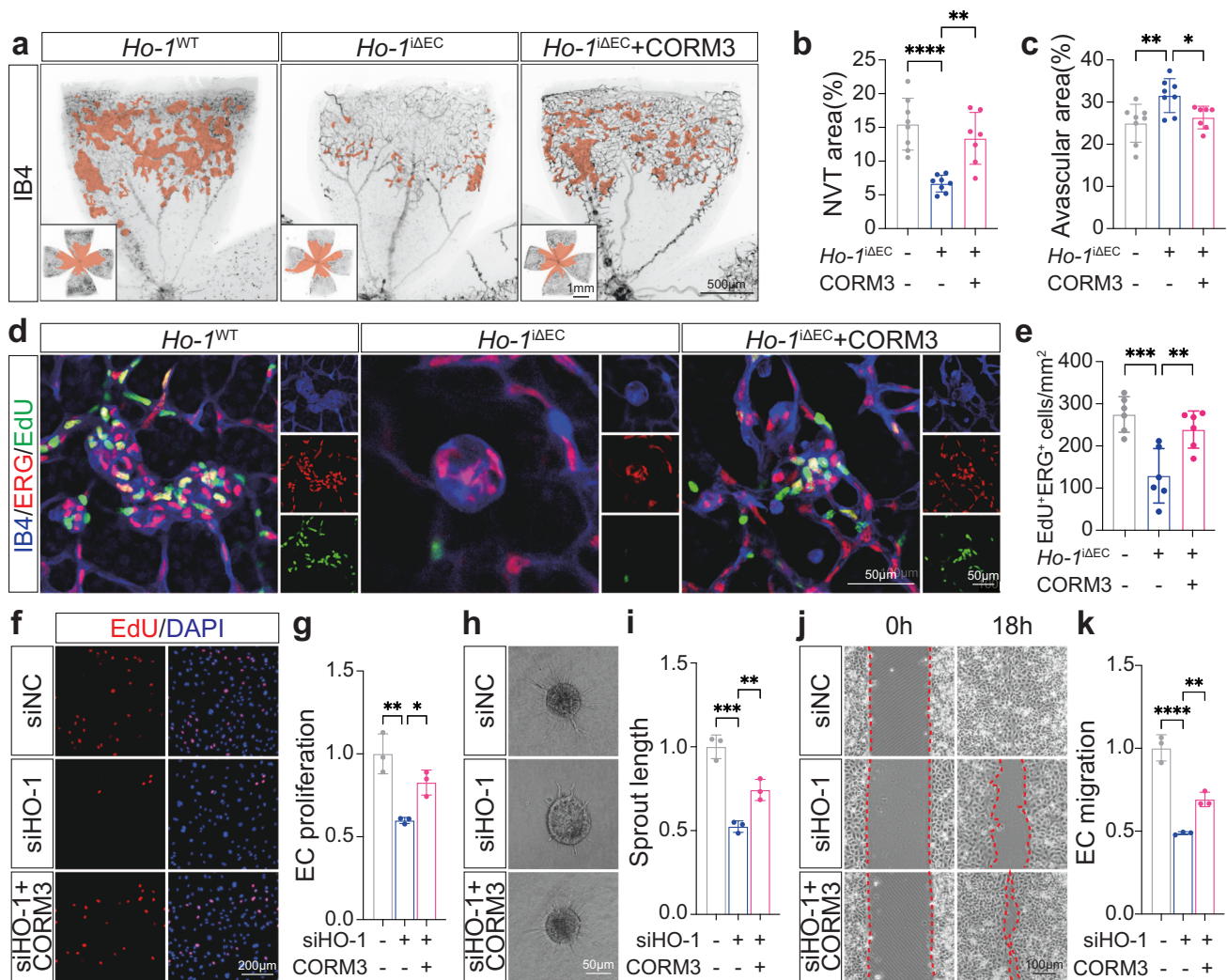


Fig. 7 | CO rescued the phenotype of *Ho-1* deletion in vitro and in vivo.

a Representative images of retinal vasculature stained with IB4 in *Ho-1*^{WT}, *Ho-1*^{ΔEC} and CORM3-treated mice at P17 using the OIR mice model. The orange space indicates the avascular area for three lower images and neovascular tufts for three upper images. Scale bar 1 mm and 500 μm. **b** Quantification of the area of neovascular tufts in the retina of *Ho-1*^{WT} ($n = 8$), *Ho-1*^{ΔEC} ($n = 8$) and CORM3-treated ($n = 7$) mice. Mean \pm SD, $p < 0.0001$, $p = 0.0017$ (one-way ANOVA with Tukey's multiple comparisons test). **c** Quantification of the avascular area in the retina of *Ho-1*^{WT} ($n = 8$), *Ho-1*^{ΔEC} ($n = 8$) and CORM3-treated ($n = 7$) mice. Mean \pm SD, $p = 0.0076$, $p = 0.0423$ (one-way ANOVA with Tukey's multiple comparisons test). **d** Immunofluorescence staining for IB4 (blue), E26 transformation-specific (ETS)-related gene (red), and EdU (green) in the retina of *Ho-1*^{ΔEC} and CORM3-treated mice. Proliferating (E26 transformation-specific (ETS)-related gene and EdU double positive) ECs are shown in yellow. Scale bar 50 μm. **e** Quantification of the proliferating ECs in the retina of *Ho-1*^{WT} ($n = 6$), *Ho-1*^{ΔEC} ($n = 6$) and CORM3-treated ($n = 6$) mice. Mean \pm SD, $p = 0.0005$, $p = 0.0056$ (one-way ANOVA with Tukey's

multiple comparisons test). **f** EdU-incorporation in *HO-1*-depleted and CORM3-treated HUVECs. DAPI (blue) identifies EC nuclei. EdU (red) staining indicates proliferating ECs. Scale bar 200 μm. **g** Quantification of EdU-incorporation in *HO-1*-depleted and CORM3-treated HUVECs. $n = 3$ replicates, and the experiments were repeated 3 times. Mean \pm SD, $p = 0.0024$, $p = 0.0341$ (one-way ANOVA with Tukey's multiple comparisons test). **h** Representative images of *HO-1*-depleted and CORM3-treated HUVECs sprouting. Scale bar 50 μm. **i** Quantification of sprouts length in *HO-1*-depleted and CORM3-treated HUVECs. $n = 3$ replicates, and the experiments were repeated 3 times. Mean \pm SD, $p = 0.0001$, $p = 0.0089$ (one-way ANOVA with Tukey's multiple comparisons test). **j** Wound healing of *HO-1*-depleted and CORM3-treated HUVECs. Scale bar 100 μm. **k** Quantification of wound healing ability in *HO-1*-depleted and CORM3-treated HUVECs. $n = 3$ replicates, and the experiments were repeated 3 times. Mean \pm SD, $p < 0.0001$, $p = 0.0075$ (one-way ANOVA with Tukey's multiple comparisons test). **** $p < 0.0001$, *** $p < 0.001$, ** $p < 0.01$, * $p < 0.05$. Source data are provided as a Source Data file.

Vascular endothelial growth factor receptor 2 (VEGFR2) is the major receptor for VEGF guiding angiogenesis⁴¹. However, VEGFR2 is widely detected in the retina, including ECs and neurons⁴². Sustained suppression of VEGF would damage the photoreceptors and lead to loss of vision^{43,44}. It is observed in the clinic that retinal atrophy occurs in patients who received anti-VEGF treatment⁴⁵. The specific expression pattern of EPCR in the retina indicates that targeting EPCR is unlikely to induce off-target effects.

It is reported that *Epcr*+ ECs are highly proliferative and major contributors to vessel development²¹. Conditional expression of diphtheria toxin (DTA) in *Epcr*+ cells delays retinal vessel extension in

postnatal mice, indicating a role for EPCR in angiogenesis²². Consistent data was acquired in our study that conditional deletion of *Epcr* in ECs suppressed the expansion of the retinal vascular plexus. Using the OIR mice model, we showed that endothelial deletion of *Epcr* or EPCR neutralization antibody reduced ECs proliferation and attenuated pathological RNV. The angiogenic role of EPCR in neovascularization is also observed in hindlimb ischemia mice⁴⁶. Deletion of *Epcr* in ECs using *Tie2-Cre; Epcr*^{fllox/fllox} mice suppresses new vessel formation⁴⁶. Given that *Epcr* transcription is specifically activated in proliferating ECs²¹, EPCR blockade could be a novel option for treating RNV with minimal effects on quiescent ECs. However, it is

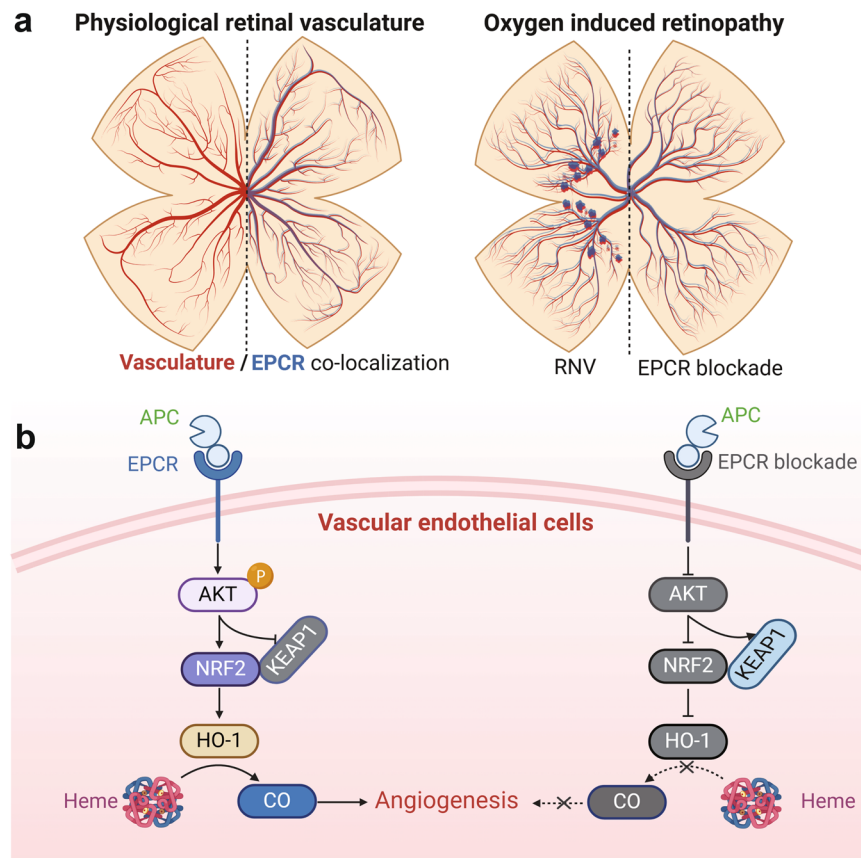


Fig. 8 | Illustration showing the expression pattern and role of EPCR during RNV. a EPCR is specifically upregulated in retinal endothelial cells during RNV, and endothelial deletion of *Epcr* ameliorates RNV. **b** EPCR regulates the

expression of HO-1 and heme catabolism-derived CO through AKT/NRF2/KEAP1 signaling. EPCR blockade decreases CO levels and inhibits retinal angiogenesis. Created in BioRender. Song, H. (2025) <https://BioRender.com/r06f399>.

also noteworthy that endothelial deletion of *Epcr* or *Ho-1* could impair the physiological vascular regeneration during OIR, as evidenced by increased vaso-oblivation observed at P17. Consistent data were acquired that inhibition of EPCR or HO-1 suppresses retinal physiological vascular development at P7. Therefore, the EPCR blocking strategy could be specific to proliferating ECs but not to pathological angiogenesis.

The mechanism by which EPCR contributes to RNV remains to be revealed. We found that the deletion of *EPCR* in ECs reduced the expression of HO-1 through the AKT/KEAP1/NRF2 pathway. In comparison, EPCR ligand (APC) treatment upregulated protein levels of HO-1 via AKT/KEAP1/NRF2. The data were consistent with studies showing that EPCR activates AKT signaling in the heart and multiple cells^{16–19}. The levels of the EPCR ligand were elevated in the serum or vitreous body of patients with PDR, suggesting that it activates EPCR signaling to favor retinal neovascularization. KEAP1 is a negative regulator of NRF2, affecting the expression of NRF2 in ECs⁴⁷. NRF2 is known to directly regulate the expression of HO-1 during tumor growth and angiogenesis^{29,48}. However, its role in retinal angiogenesis is complex. NRF2 is detected in retinal ganglion cells, astrocytes, müller glial cells, and ECs, with prominent expression in retinal ganglion cells and müller glial cells during retinopathy^{49,50}. Enhancing NRF2 activity in retinal neurons can attenuate diabetic retinopathy and inhibit RNV⁴⁹. Meanwhile, endothelial deletion of *Nrf2* delays vascular expansion and decreases vascular density⁵¹. Our data showed that the deletion of *EPCR* in ECs decreased the protein levels of NRF2 and HO-1 and inhibited the angiogenic function of ECs. These results indicate a notable difference in the cellular context of NRF2 action, and NRF2 plays a vital role in regulating HO-1 after endothelial deletion of *EPCR*.

Here, we showed that EC-specific deletion of *Ho-1* suppressed retinal neovascularization in OIR and postnatal mice's retina. HO-1 catalyzes heme degradation to CO, ferrous iron, and biliverdin⁵². While initially considered a waste product, CO is increasingly recognized as a cytoprotective and homeostatic molecule⁵³. Heme catabolism-derived CO is a major source of endogenous CO⁵⁴, which contributes to tumor metastasis and angiogenesis³⁷. In ECs, CO is reported to increase cell growth in vitro, whereas its role in vivo is unknown³⁸. Here, our data indicate that heme catabolism-derived CO promoted retinal angiogenesis, revealing a vital role of CO in angiogenesis. Clinically, the levels of exhaled CO significantly increase in patients with diabetes and correlate with blood glucose levels and disease duration^{55,56}. PDR, characterized by uncontrolled RNV, is a late-stage microvascular complication of diabetes³. Elevated levels of APC in the serum or vitreous body of patients with PDR could activate EPCR signaling. This data suggests that this upregulated EPCR signaling may enhance heme catabolism and increase CO production, potentially contributing to RNV. However, the precise roles of EPCR and heme catabolism in the retinas of patients with PDR require further investigation.

In summary, we determined that EPCR is highly expressed in retinal ECs and that blocking EPCR attenuates pathological retinal angiogenesis. Mechanistically, EPCR controls heme catabolism via the KEAP1/NRF2/HO-1 pathway, and CO derived from heme catabolism plays a vital role in RNV. Hence, our findings elucidate a novel mechanism of RNV and suggest that EPCR may be a promising therapeutic target for translational application. However, these mouse models do not accurately represent the pathological progression of retinopathy in primates. Therefore, determining the therapeutic efficiency of anti-EPCR for pathological retinal angiogenesis in non-human

primates is indispensable in the future. Moreover, the expression pattern of EPCR in the human retina is unknown. For translational significance, it is important to determine the expression pattern of EPCR in post-mortem retinas under diverse pathophysiological conditions.

Methods

Patient samples

The patients diagnosed with proliferative diabetic retinopathy (PDR), idiopathic epiretinal membrane (ERM), and idiopathic macular hole (MH) were included. Vitreous samples were obtained from patients who underwent vitrectomy surgery by the same surgeon. Details of the patient information are shown in Supplementary Table 1. The collected vitreous samples were placed on ice immediately and centrifuged to exclude the debris. The supernatants were aliquoted into sterile tubes and stored in liquid nitrogen. Serum samples were obtained from patients who were diagnosed with PDR. The control serum samples were obtained from patients who were diagnosed with ERM and MH. Details of the patient information are shown in Supplementary Table 2. The obtained serum samples were centrifuged at 4 °C, and the supernatants were stored at -80 °C. All surgeries were performed, and human samples were harvested in accordance with the principles in the Declaration of Helsinki. This study was approved by the institutional research ethics committee of Shanghai General Hospital ([2022]-109). Individuals provided written informed consent prior to their participation in the study.

Mice

All the experimental animals were accommodated in animal facilities, where they were subjected to 12-hour cycles of light and darkness. These animals were provided with unrestricted access to standard chow and water. The C57BL/6J mice were purchased from Jihui Laboratory Animal Care Co., Ltd. *Epcr*^{flx/flx} mice (the Cyagen Biotechnology Co., Ltd.) and *Ho-1*^{flx/flx} mice (the Cyagen Biotechnology Co., Ltd.) were crossed with *Cdh5* CreER^{T2} mice⁵⁷ respectively to generate conditional knockout mice. For the lineage tracing of *Epcr*⁺ cells, the *Epcr* CreER^{T2} mice²¹ were crossed to *Rosa26*^{tdTomato} reporter mice (the Cyagen Biotechnology Co., Ltd.) The body weight measurement and body weight analysis of mice were shown in Supplementary Table 3, 4. All animal studies were approved by the Institutional Animal Care and Use Committee at Shanghai Changhai Hospital (CHEC (A.E) 2023-024).

Oxygen-induced retinopathy (OIR)

Oxygen-induced retinopathy (OIR) was performed as previously reported²⁵. In brief, the pups were exposed to 75% oxygen with their nursing mothers for five days from P7 to P12. Then, the pups were returned to room air at P12. When the mice were returned to room air, the hypoxia-induced neovascularization was initiated and peaked on P17. Animals were euthanized, and the retinas were harvested at P17. To activate CreER^{T2}, 50 µl of tamoxifen (2 mg/ml) was injected intraperitoneally from P10 to P12. To evaluate the anti-angiogenic role of EPCR neutralizing antibody, mice were randomly divided into three groups and injected intravitreally with 1 µl anti-EPCR antibody, PBS, and anti-IgG, respectively, at P12. Ocular surface anesthesia was performed using one drop of 0.5% proparacaine hydrochloride (ALCON-COUVREUR N.V.) before injection. ZnPPiX (25 mg/kg) and CORM3 (40 mg/kg) were injected intraperitoneally twice at P12 and P13. To detect proliferating cells, 50 µl EdU (50 mg/kg) was administered intraperitoneally 6 h before euthanasia. The neovascular tuft and avascular areas were measured using the Freehand selection and Measurement tools in Image J software and then divided by the total retinal area. Mice (P17) with body weight lower than 6 g were excluded from the analysis.

RNA-Seq sample preparation and sequencing

Total RNA from retinas and cells was extracted with RNA Easy Fast Tissue/Cell Kit (TIANGEN). Agilent 2100 Bioanalyzer and RNA nano 6000 assay kit (Agilent Technologies) were used to evaluate the quality of RNA samples. The transcriptome sequencing library was constructed through 1 ng/µl RNA randomly fragmentation, cDNA strand 1 / strand 2 synthesis, end repair, A-tailing, ligation of sequencing adapters, size selection, and library PCR enrichment. The integrity of cDNA was evaluated by Agilent 2100 Bioanalyzer. The library preparations were sequenced on an Illumina HiSeq 2500 platform (Illumina, USA). The raw data of sequences were uploaded to the NCBI Sequence Read Archive (SRA) database (GSE241239 for the retinas of OIR mice; GSE249130 for HUVECs with *EPCR* deletion).

Isolation of retinal ECs

Isolation of retinal ECs was performed according to protocols we previously described with some modifications²¹. The retinas were separated from eyeballs then minced into fine fragments and digested in Iscove's Modified Dulbecco's Medium (IMDM, LI1090-500, BioA-grio) with 1.5 mg/ml Collagenase H (11087789001, Roche), 1.25 mM CaCl₂, 0.4 mM MgCl₂, 1% penicillin/streptomycin and 3.5 µg/ml DNaseI (D4263, Sigma) at 37 °C for 45 min. The samples were pipetted every 10 min using a 1 ml pipette tip to ensure even digestion. The digestion mix was passed through a 40 µm nylon mesh to prepare single-cell suspensions. Cells were then incubated for 20 min with FITC-conjugated anti-CD31 (11-0317-82, Invitrogen, diluted 1:100) and PE-Cy7 conjugated anti-CD45 (25-0451-82, Invitrogen, diluted 1:200) in PBS with 5% FBS. Then, the single-cell suspensions were subjected to FACS using SONY ID7000 or LSR Fortessa (BD Biosciences). FACS data were analyzed by FlowJo software. The purity of sorted ECs was routinely checked and ensured to be more than 95%.

Real-time PCR analysis

Retinas were homogenized completely through a tissue grinding apparatus (Bioprep-24R, ALLSHEG). Total RNA was extracted from homogenized retina and HUVECs using MolPure® TRIeasy Plus Total RNA Kit (19211ES60, YEASEN). cDNA was prepared using Hifair® III 1st Strand cDNA Synthesis SuperMix for qPCR (11141ES, YEASEN) following manufacturer instructions. Quantitative PCR performed with Hieff UNICON® Universal Blue qPCR AYBR Green Master Mix (11184ES, YEASEN) in Bio-Rad CFX Manager 2.1 Detection system (Bio-Rad, Hercules, CA, USA). Relative gene expression was calculated with the $\Delta\Delta$ CT method and normalized to the expression of β -actin. Primer sequences are provided in Supplementary Table 5.

Retinal dissection and whole-mount staining

Eyes were fixed in 4% paraformaldehyde (PFA) for 0.5 h at RT. After dissection, retinas were blocked in a blocking buffer (1% BSA, 5% FBS, and 0.5% Triton-X-100 in PBS) for 1 h at RT. Primary antibodies were diluted in PBS containing 1% BSA and incubated with the retinas at 4 °C overnight. After being washed twice with PBS, retinas were incubated with secondary antibodies at RT for 2 h. Then, the retinas were washed and flat-mounted with Fluoromount-G (SouthernBiotech). For the labeling of EdU, an additional step was performed to detect EdU-labeled proliferative cells using the Click-It EdU kit (C10338, Invitrogen) prior to mounting. Images were acquired with a Mica confocal microscope (Leica Microsystems). For the quantification of proliferating ECs in the OIR model, high-resolution confocal images (20x magnification) of IB4, ERG, and EdU labeled retinal vasculature were acquired. Four fields were taken for quantification per retina, and the total number of EdU and ERG double-positive cells were counted by image-J software per field. Then, the mean of each retina was calculated subsequently. The mean from each group was statistically compared using GraphPad Prism, and a student's t-test was performed to calculate the *p*-value.

Quantification and statistical analysis

All calculations were performed using GraphPad Prism (GraphPad software 9.0, GraphPad, Bethesda, MD, USA). Statistical analysis was performed using the two-tailed Student's t-test and one-way analysis of variance (ANOVA), where appropriate, to compare different groups. For all bar graphs, data were presented as mean \pm SD. All experiments were repeated at least three times, and *P* values of <0.05 were considered as statistically significant.

Reporting summary

Further information on research design is available in the Nature Portfolio Reporting Summary linked to this article.

Data availability

The datasets generated during the current study are available in the GEO repository, GSE 241239 and GSE 249130. Source data are provided with this paper. The RNA-seq data generated in this study have been deposited in the Gene Expression Omnibus (GEO) under accession code GSE 241239 and GSE 249130. Source data are provided with this paper.

References

- Binet, F. et al. Neutrophil extracellular traps target senescent vasculature for tissue remodeling in retinopathy. *Science* **369**, (2020).
- Camposchiari, P. A. Molecular pathogenesis of retinal and choroidal vascular diseases. *Prog. Retin Eye Res* **49**, 67–81 (2015).
- Antoszyk, A. N. et al. Effect of intravitreal aflibercept vs vitrectomy with panretinal photocoagulation on visual acuity in patients with vitreous hemorrhage from proliferative diabetic retinopathy: a randomized clinical trial. *Jama* **324**, 2383–2395 (2020).
- Stahl, A. et al. Effect of intravitreal aflibercept vs laser photocoagulation on treatment success of retinopathy of prematurity: the FIREFLYE randomized clinical trial. *Jama* **328**, 348–359 (2022).
- Yeh, S. et al. Therapies for macular edema associated with central retinal vein occlusion: a report by the American Academy of Ophthalmology. *Ophthalmology* **122**, 769–778 (2015).
- Gariano, R. F. & Gardner, T. W. Retinal angiogenesis in development and disease. *Nature* **438**, 960–966 (2005).
- Selvam, S., Kumar, T. & Fruttiger, M. Retinal vasculature development in health and disease. *Prog. Retin Eye Res* **63**, 1–19 (2018).
- Eelen, G., Treps, L., Li, X. & Carmeliet, P. Basic and therapeutic aspects of angiogenesis updated. *Circ. Res* **127**, 310–329 (2020).
- Apte, R. S., Chen, D. S. & Ferrara, N. VEGF in signaling and disease: beyond discovery and development. *Cell* **176**, 1248–1264 (2019).
- Simons, M., Gordon, E. & Claesson-Welsh, L. Mechanisms and regulation of endothelial VEGF receptor signalling. *Nat. Rev. Mol. Cell Biol.* **17**, 611–625 (2016).
- Arima, M. et al. Claudin-5 redistribution induced by inflammation leads to anti-VEGF-resistant Diabetic Macular Edema. *Diabetes* **69**, 981–999 (2020).
- Wallsh, J. O. & Gallempore, R. P. Anti-VEGF-resistant retinal diseases: a review of the latest treatment options. *Cells* **10**, 1049 (2021).
- Wang, D. et al. Long-term expansion of pancreatic islet organoids from resident procr(+) progenitors. *Cell* **180**, 1198–1211.e1119 (2020).
- Mohan Rao, L. V., Esmo, C. T. & Pendurthi, U. R. Endothelial cell protein C receptor: a multiliganded and multifunctional receptor. *Blood* **124**, 1553–1562 (2014).
- Magisetty, J. et al. Selective inhibition of activated protein C anticoagulant activity protects against hemophilic arthropathy in mice. *Blood* **139**, 2830–2841 (2022).
- Ren, D. et al. Activated protein C strengthens cardiac tolerance to ischemic insults in aging. *Circ. Res* **130**, 252–272 (2022).
- Yang, X. V. et al. Activated protein C ligation of ApoER2 (LRP8) causes Dab1-dependent signaling in U937 cells. *Proc. Natl Acad. Sci. USA* **106**, 274–279 (2009).
- Sinha, R. K. et al. Apolipoprotein E receptor 2 mediates activated protein C-induced endothelial AKT activation and endothelial barrier stabilization. *Arterioscler Thromb. Vasc. Biol.* **36**, 518–524 (2016).
- Wang, D. et al. Protein C receptor stimulates multiple signaling pathways in breast cancer cells. *J. Biol. Chem.* **293**, 1413–1424 (2018).
- Wang, D. et al. Protein C receptor is a therapeutic stem cell target in a distinct group of breast cancers. *Cell Res* **29**, 832–845 (2019).
- Yu, Q. C. et al. Activation of Wnt/ β -catenin signaling by Zeb1 in endothelial progenitors induces vascular quiescence entry. *Cell Rep.* **41**, 111694 (2022).
- Yu, Q. C., Song, W., Wang, D. & Zeng, Y. A. Identification of blood vascular endothelial stem cells by the expression of protein C receptor. *Cell Res* **26**, 1079–1098 (2016).
- Connor, K. M. et al. Quantification of oxygen-induced retinopathy in the mouse: a model of vessel loss, vessel regrowth and pathological angiogenesis. *Nat. Protoc.* **4**, 1565–1573 (2009).
- Zou, J. et al. Interleukin-19 promotes retinal neovascularization in a mouse model of oxygen-induced retinopathy. *Invest Ophthalmol. Vis. Sci.* **63**, 9 (2022).
- Crespo-Garcia, S. et al. Pathological angiogenesis in retinopathy engages cellular senescence and is amenable to therapeutic elimination via BCL-xL inhibition. *Cell Metab.* **33**, 818–832.e817 (2021).
- Caprara, C. & Grimm, C. From oxygen to erythropoietin: relevance of hypoxia for retinal development, health and disease. *Prog. Retin Eye Res* **31**, 89–119 (2012).
- Brash, J. T. et al. Tamoxifen-activated CreERT impairs retinal angiogenesis independently of gene deletion. *Circ. Res* **127**, 849–850 (2020).
- Liu, C. et al. Procr functions as a signaling receptor and is essential for the maintenance and self-renewal of mammary stem cells. *Cell Rep.* **38**, 110548 (2022).
- Lignitto, L. et al. Nrf2 activation promotes lung cancer metastasis by inhibiting the degradation of Bach1. *Cell* **178**, 316–329.e318 (2019).
- Mills, E. L. et al. Itaconate is an anti-inflammatory metabolite that activates Nrf2 via alkylation of KEAP1. *Nature* **556**, 113–117 (2018).
- Dai, X. et al. Elevating CXCR7 improves angiogenic function of EPCs via Akt/GSK-3 β /Fyn-mediated Nrf2 activation in diabetic limb ischemia. *Circ. Res* **120**, e7–e23 (2017).
- Lien, E. C. et al. Glutathione biosynthesis is a metabolic vulnerability in PI(3)K/Akt-driven breast cancer. *Nat. Cell Biol.* **18**, 572–578 (2016).
- Deshane, J. et al. Stromal cell-derived factor 1 promotes angiogenesis via a heme oxygenase 1-dependent mechanism. *J. Exp. Med.* **204**, 605–618 (2007).
- Butler, J. M. et al. SDF-1 is both necessary and sufficient to promote proliferative retinopathy. *J. Clin. Invest* **115**, 86–93 (2005).
- Lima e Silva, R. et al. The SDF-1/CXCR4 ligand/receptor pair is an important contributor to several types of ocular neovascularization. *Faseb j.* **21**, 3219–3230 (2007).
- Otterbein, L. E., Soares, M. P., Yamashita, K. & Bach, F. H. Heme oxygenase-1: unleashing the protective properties of heme. *Trends Immunol.* **24**, 449–455 (2003).
- Consonni, F. M. et al. Heme catabolism by tumor-associated macrophages controls metastasis formation. *Nat. Immunol.* **22**, 595–606 (2021).
- Dulak, J., Deshane, J., Jozkowicz, A. & Agarwal, A. Heme oxygenase-1 and carbon monoxide in vascular pathobiology: focus on angiogenesis. *Circulation* **117**, 231–241 (2008).
- Loboda, A., Jozkowicz, A. & Dulak, J. HO-1/CO system in tumor growth, angiogenesis and metabolism - Targeting HO-1 as an anti-tumor therapy. *Vasc. Pharm.* **74**, 11–22 (2015).
- Fogli, S. et al. Clinical pharmacology of intravitreal anti-VEGF drugs. *Eye (Lond.)* **32**, 1010–1020 (2018).

41. Pérez-Gutiérrez, L., Ferrara, N. Biology and therapeutic targeting of vascular endothelial growth factor A. *Nat Rev Mol Cell Biol* (2023).
42. Okabe, K. et al. Neurons limit angiogenesis by titrating VEGF in retina. *Cell* **159**, 584–596 (2014).
43. Usui, Y. et al. Neurovascular crosstalk between interneurons and capillaries is required for vision. *J. Clin. Invest* **125**, 2335–2346 (2015).
44. Bucher, F. et al. Antibody-mediated inhibition of tspan12 ameliorates vasoproliferative retinopathy through suppression of β -catenin signaling. *Circulation* **136**, 180–195 (2017).
45. Sadda, S. R., Guymer, R., Monés, J. M., Tufail, A. & Jaffe, G. J. Anti-vascular endothelial growth factor use and atrophy in neovascular age-related macular degeneration: systematic literature review and expert opinion. *Ophthalmology* **127**, 648–659 (2020).
46. Bochenek, M. L. et al. EPCR-PAR1 biased signaling regulates perfusion recovery and neovascularization in peripheral ischemia. *JCI Insight* **7** (2022).
47. Kopacz, A. et al. Keap1 governs ageing-induced protein aggregation in endothelial cells. *Redox Biol.* **34**, 101572 (2020).
48. Huang, Z. et al. Nattokinase attenuates retinal neovascularization via modulation of Nrf2/HO-1 and glial activation. *Invest Ophthalmol. Vis. Sci.* **62**, 25 (2021).
49. Wei, Y. et al. Nrf2 in ischemic neurons promotes retinal vascular regeneration through regulation of semaphorin 6A. *Proc. Natl Acad. Sci. USA* **112**, E6927–E6936 (2015).
50. Xu, Z. et al. NRF2 plays a protective role in diabetic retinopathy in mice. *Diabetologia* **57**, 204–213 (2014).
51. Wei, Y. et al. Nrf2 acts cell-autonomously in endothelium to regulate tip cell formation and vascular branching. *Proc. Natl Acad. Sci. USA* **110**, E3910–E3918 (2013).
52. Ayer, A., Zarjou, A., Agarwal, A. & Stocker, R. Heme oxygenases in cardiovascular health and disease. *Physiological Rev.* **96**, 1449–1508 (2016).
53. Yuan, Z., De La Cruz, L. K., Yang, X. & Wang, B. Carbon monoxide signaling: examining its engagement with various molecular targets in the context of binding affinity, concentration, and biologic response. *Pharm. Rev.* **74**, 823–873 (2022).
54. Otterbein, L. E., Foresti, R. & Motterlini, R. Heme oxygenase-1 and carbon monoxide in the heart: the balancing act between danger signaling and pro-survival. *Cir. c. Res* **118**, 1940–1959 (2016).
55. Paredi, P., Biernacki, W., Invernizzi, G., Kharitonov, S. A. & Barnes, P. J. Exhaled carbon monoxide levels elevated in diabetes and correlated with glucose concentration in blood: a new test for monitoring the disease? *Chest* **116**, 1007–1011 (1999).
56. Cheng, S. et al. Exhaled carbon monoxide and risk of metabolic syndrome and cardiovascular disease in the community. *Circulation* **122**, 1470–1477 (2010).
57. Wang, Y. et al. Ephrin-B2 controls VEGF-induced angiogenesis and lymphangiogenesis. *Nature* **465**, 483–486 (2010).

Acknowledgements

Thanks to Yi Ariel Zeng (State Key Laboratory of Cell Biology, Chinese Academy of Sciences) for kindly providing *Epcr-CreER^{T2}* mice and technical assistance; to Youheng Wei (State Key Laboratory of Genetic Engineering, Fudan University, Shanghai, China) for providing technical assistance. This work was supported by grants from National Natural

Science Foundation of China (82171081, 82271106, 82388101, U22A20311, 82171076), National Key R&D Program (2022YFC2502800), Shanghai Municipal Education Commission (2023ZKZD18), Shanghai Science and Technology Committee (22ZR1478200), Shanghai Changhai Hospital (2023YQ01). Figure 1a, Fig. 8, and Supplementary Fig. 1d, j were created using BioRender.com.

Author contributions

Conceptualization, H.S., X.D.S., W.S., H.J.Z., and F.L.; Methodology, Q.L., X.S., and A.G.; investigation, H.S., Q.L., X.G., Z.F., W.Z., M.W., Y.L., H.R.Z., Z.N., L.Z., H.M.Z., and Y.J.; Funding acquisition, X.D.S., H.S. and W.S.; Writing-original draft, H.S. and Q.L.; Writing-review & editing, X.D.S., F.Z., F.L., and X.L.; Supervision, H.S., X.D.S., X.L. and F.Z. All authors approved the final version of the manuscript.

Competing interests

The authors declare no competing interests.

Additional information

Supplementary information The online version contains supplementary material available at <https://doi.org/10.1038/s41467-025-56810-0>.

Correspondence and requests for materials should be addressed to Hongyuan Song, Fanyan Luo, Hongjian Zhang, Wei Shen or Xiaodong Sun.

Peer review information *Nature Communications* thanks Jian-xing Ma, Abolfazl Zarjou and the other, anonymous, reviewer(s) for their contribution to the peer review of this work. A peer review file is available.

Reprints and permissions information is available at <http://www.nature.com/reprints>

Publisher's note Springer Nature remains neutral with regard to jurisdictional claims in published maps and institutional affiliations.

Open Access This article is licensed under a Creative Commons Attribution-NonCommercial-NoDerivatives 4.0 International License, which permits any non-commercial use, sharing, distribution and reproduction in any medium or format, as long as you give appropriate credit to the original author(s) and the source, provide a link to the Creative Commons licence, and indicate if you modified the licensed material. You do not have permission under this licence to share adapted material derived from this article or parts of it. The images or other third party material in this article are included in the article's Creative Commons licence, unless indicated otherwise in a credit line to the material. If material is not included in the article's Creative Commons licence and your intended use is not permitted by statutory regulation or exceeds the permitted use, you will need to obtain permission directly from the copyright holder. To view a copy of this licence, visit <http://creativecommons.org/licenses/by-nc-nd/4.0/>.

© The Author(s) 2025